ADVANCED FUNCTIONAL MATERIALS
www.afm-journal.de

Materials Views
www.MaterialsViews.com

Ambient Layer-by-Layer ZnO Assembly for Highly Efficient Polymer Bulk Heterojunction Solar Cells

*Mohamed Eita, Abdulrahman El Labban, Federico Cruciani, Anwar Usman, Pierre M. Beaujuge, and Omar F. Mohammed**

The use of metal oxide interlayers in polymer solar cells has great potential because metal oxides are abundant, thermally stable, and can be used in flexible devices. Here, a layer-by-layer (LbL) protocol is reported as a facile, room-temperature, solution-processed method to prepare electron transport layers from commercial ZnO nanoparticles and polyacrylic acid (PAA) with a controlled and tunable porous structure, which provides large interfacial contacts with the active layer. Applying the LbL approach to bulk heterojunction polymer solar cells with an optimized ZnO layer thickness of ≈25 nm yields solar cell power-conversion efficiencies (PCEs) of ≈6%, exceeding the efficiency of amorphous ZnO interlayers formed by conventional sputtering methods. Interestingly, annealing the ZnO/PAA interlayers in nitrogen and air environments in the range of 60–300 °C reduces the device PCEs by almost 20% to 50%, indicating the importance of conformational changes inherent to the PAA polymer in the LbL-deposited films to solar cell performance. This protocol suggests a new fabrication method for solution-processed polymer solar cell devices that does not require postprocessing thermal annealing treatments and that is applicable to flexible devices printed on plastic substrates.

1. Introduction

Thin-film solar cell technologies are being developed for efficient, renewable, and economically attractive large-scale energy production and to reduce greenhouse gas emissions.[1–4] The development of thin-film solar cells has been based on electron-donor and electron-acceptor materials made from metal oxides,[5] small-molecule chromophores,[6,7] macromolecules,[8] polymers,[9,10] and quantum dots.[11–13] In donor–acceptor systems, the energy conversion efficiency is strongly dependent on the interfacial contact between the donor and the acceptor components. The architecture of a solar cell can thus provide an efficient thermodynamic driving force to dissociate a strongly bound exciton and to drive electron-transfer processes.

Dr. M. Eita, Dr. A. E. Labban, F. Cruciani, Dr. A. Usman, Prof. P. M. Beaujuge, Prof. O. F. Mohammed
Solar and Photovoltaics Engineering Research Center (SPERC)
Division of Physical Sciences and Engineering
King Abdullah University of Science and Technology
Thuwal 23955–6900, Saudi Arabia
E-mail: omar.abdelsaboor@kaust.edu.sa

DOI: 10.1002/adfm.201402637

To produce printable, portable, and flexible bulk heterojunction (BHJ) solar cells, the development of efficient, inexpensive, and high-throughput fabrication methods is critically important. A number of methods to fabricate BHJ solar cells already exist, including high-vacuum deposition systems, solution processing, and direct chemical deposition on device substrates.[5,14–16] Because solution processing is amenable to the formation of an interpenetrating donor–acceptor network, while also being a cost-effective approach, it is one of the most promising approaches to large-scale BHJ solar cell modules.[15,16] Among various solution processable donor–acceptor systems, polymer BHJ solar cells based on interpenetrating networks of conjugated polymer and fullerene derivatives as donor and acceptor materials have exhibited a power conversion efficiency (PCE) up to ≈10%.[17–20] This dramatic increase in photovoltaic performance is caused by the optimization of the morphology of the active layer, the device architecture, and the interface control of the electron donors and acceptors. The other important approach to optimizing the interpenetrating networks and interfacial contacts between the donor and acceptor components is the use of hybrid polymer-metal oxides, in which the polymer acts as the light-absorbing component.[15,21–24] One of the key issues associated with the polymer-metal oxide BHJ solar cells is the high electron mobilities in the inorganic component compared with the modest hole mobilities in the polymer. Efficient polymer-metal oxide BHJ solar cells have been demonstrated using ZnO nanoparticles and a conducting polymer, such as a poly-1,4-phenylenevinylene derivative.[15,22] For instance, under AM1.5 conditions, polymer/ZnO solar cells with short circuit current densities (J_{SC}) of 3.3 mA cm^{-2}, open circuit voltages (V_{OC}) of 0.81 V, fill factors (FF) of ≈60%, and overall PCE of 1.6% have been reported.[15] This finding indicates that ZnO, an *n*-type metal oxide, possessing a wide direct bandgap (3.37 eV), an appropriate conduction band, and high electron-transporting properties, is an effective electron transport layer (ETL) for inverted polymer solar cells.[25–27] The strong absorption of ZnO in the UV region with a band edge cut-off at 370 nm is also important to blocking UV light and protecting the photoactive layer.[28]

Though ZnO ETL for solar cells generally can be prepared by various methods, such as atomic layer deposition,[29] electro deposition,[25] spin-coating,[30] spray-coating,[31] and the sol-gel technique,[26,32] it is well known that low-temperature solution-processed amorphous ZnO layers usually yield poor device performance with a reported maximum PCE of ≈3.2%.[31] This indicates that low-temperature processing of ZnO may introduce substantial microstructural and/or morphological imperfections into the donor-acceptor network, which could be detrimental to many applications. Thus, ordered ZnO nanorods or crystalline ZnO films with optimized morphological and microstructural features and high carrier mobilities have been proposed to improve the performance of conducting polymer-ZnO nanoparticles (NP) BHJ solar cells.[22,25,31–33] Recently, solution-processed amorphous ZnO interlayers prepared at low temperatures (100 °C) in inverted BHJ solar cells have been demonstrated to have a power conversion efficiency of ≈4.1%, as efficient as solar cells based on polycrystalline ZnO films prepared at substantially higher temperatures (150–400 °C).[34] On the other hand, room-temperature fabrication of ZnO ETL by spin-coating perovskite solar cells has also been reported, indicating that even annealing was not required.[35] The marked efficiency of ZnO ETL fabricated at room temperature is due most probably to its crystal structure, which differs from the crystal structures fabricated by annealing.[31] These findings suggest that low-temperature, facile solution processing approaches are possible in the fabrication of BHJ solar cells on flexible plastic substrates. Under such processing conditions, however, the interfacial contacts between the donor and the acceptor units, which are needed to optimize the conversion efficiency, cannot be controlled. An alternative technique that can be used to control the interfacial contacts is the room-temperature layer-by-layer (LbL) method. Using this method, we created porous structures within the ZnO NP layers on which quantum dots, for example, could be incorporated as the light absorber layer.[36]

Here, we describe the assembly and performance of a ZnO NPs/poly(benzo[1,2-b:4,5-b′]dithiophene-thieno[3,4-c]pyrrole-4,6-dione) (PBDTTPD)/[6,6]-phenyl C_{61} butyric acid methyl ester (PCBM) BHJ solar cell with the device architecture shown in **Figure 1**. We prepared the ZnO-based ETL by using a LbL approach based on a ZnO/polyacrylic acid (PAA) multilayered structure deposited from aqueous solutions. This approach allowed the ZnO/PAA thickness and the porous structure to be tuneable.[36] We examined the film build-up and surface morphology of the ZnO ETL by ellipsometry and atomic force microscopy (AFM). We made the polymer-fullerene BHJ device by simply spin-coating an active layer of PBDTTPD and PCBM onto the LbL-deposited ZnO/PAA thin film. We note that PBDTTPDs are among the best-performing polymer donors for BHJ solar cells with PCBM acceptors, yielding high V_{OC} >0.9 V, high FFs of ≈70%, and PCEs >6% in direct device configurations.[37–43] We used PBDTTPD-based BHJ solar cells as a model system to show that the performance of inverted BHJ devices with ZnO-based interlayers depends on the thickness of the ZnO layer deposited by the LbL approach. We show that as-prepared LbL-deposited ZnO/PAA solar cells yield comparably high figures of merit: J_{SC} as high as 12.4 mA cm^{-2}, V_{OC} of 0.87 V, FF of 55%, and PCE of 6.0% at an optimized ZnO layer thickness of 25 nm. Interestingly, the performance of our as-prepared BHJ solar cells at room temperature was better than that of thermally annealed devices, indicating the importance of conformational changes of the PAA polymer in the LbL-deposited films to solar cell performance.

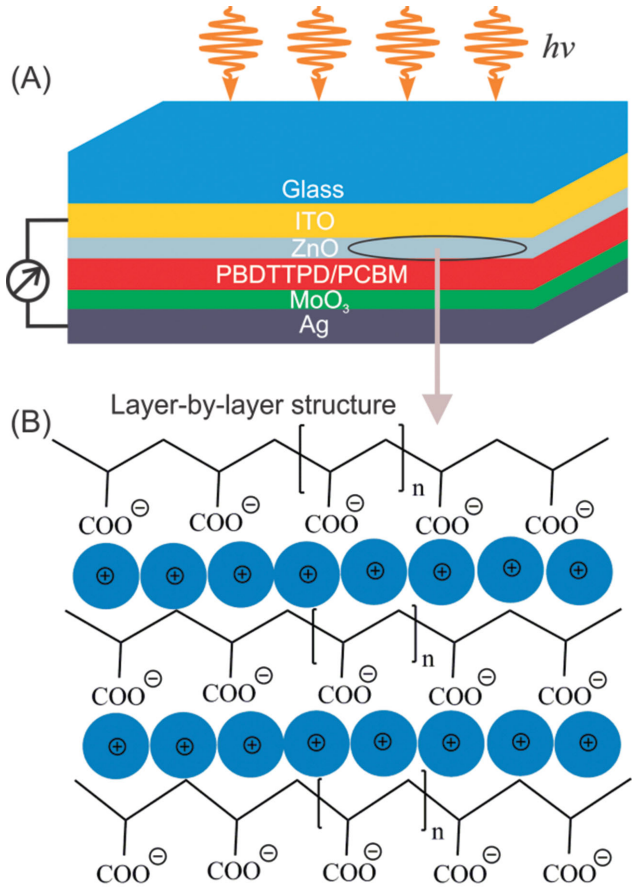

Figure 1. a) The device architecture of a layer-by-layer ZnO NP/poly(benzo[1,2-b:4,5-b′]dithiophene-thieno[3,4-c]pyrrole-4,6-dione) (PBDTTPD)/[6,6]-phenyl C_{61} butyric acid methyl ester (PCBM) ordered bulk hetero-junction solar cell. b) The layer-by-layer structure consisting of multilayers of polyacrylic acid (PAA) and ZnO nanoparticles.

2. Results and Discussion

2.1. Preparation of the ZnO ETL

We prepared thin films of ZnO/PAA ETL under optimized conditions according to a previously described LbL method for implementation in polymer BHJ devices.[36,44] **Figure 2**a shows the film thickness as a function of the number of ZnO/PAA bilayers as measured by ellipsometry, demonstrating a progressive thickness variation starting at 13 nm for one bilayer and reaching 29 nm for five bilayers. AFM height images for one and five bilayer(s) are shown in Figure 2b,c, respectively. In the one-bilayer thin film, the ZnO NPs cover the substrate in a densely packed manner. In addition, we also measured the

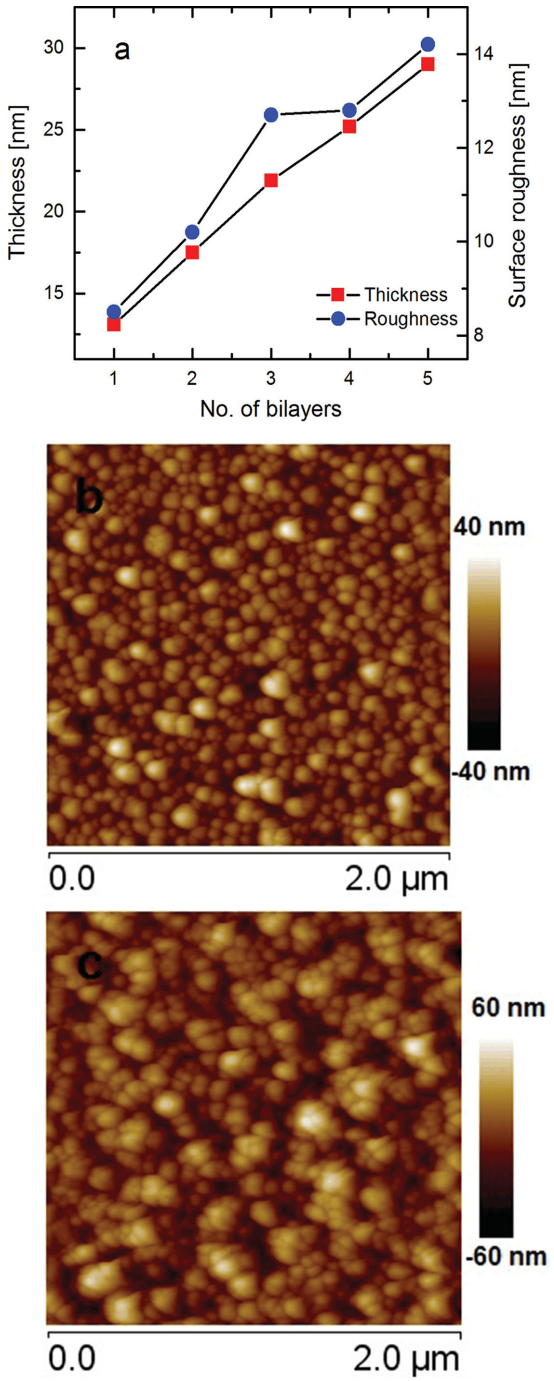

Figure 2. a) Changes in the thickness and root mean square (RMS) roughness of the surface with increasing number of bilayers, b,c) AFM height images of one bilayer and five bilayers of ZnO/PAA thin films, respectively, on silica substrates.

film thickness by AFM step analysis for comparison, and we found that the thicknesses of the one and five bilayer samples is approximated ≈12 and ≈30 nm, respectively, (Figure S1, Supporting Information) which are comparable to those measured by ellipsometry.

The ZnO NPs are irregular in shapes with sizes of ≈20 nm as apparent in transmission electron microscopy (TEM) image (Figure S2, Supporting Information). whereas the hydrodynamic radius is 99 nm as measured by dynamic light scattering (DLS) in solution.[44] These results suggest that ZnO NPs are always associated with water and surfactant molecules, and hence several associated ZnO NPs co-adsorb together onto the surface as seen in the AFM image. By increasing the number of bilayers, the nanoparticles tend to assemble to form a nanoporous structure as seen in the AFM image in Figure 2c. The surface roughness as measured by AFM increases as the number of bilayers increases as shown in Figure 2a. Apparently, the surface roughness is high at a given film thickness, e.g., the five-bilayer film is 29 nm thick while its surface roughness is 14.2 nm. The overall thickness of the film is lower compared to the average particle size of ZnO NPs. This observation was reported previously and is due to imperfections in the multilayer structure.[44] Adsorption happens at the beginning of the process in separate domains. The porous structure is hence formed from the beginning. By increasing the number of bilayers, the porous structure grows and thus the overall film thickness is low. Given that ZnO nanoparticles are granular and not spherical (Figure S2, Supporting Information), the film build-up is not a consequence of the particle size in the *Z*-direction. There is a three-dimensional build-up of granules that could fit everywhere in the porous structure rather than growing only in the *Z*-direction giving rise to the low thickness reported by ellipsometry (Figure 2a) and by AFM (Figure S1, Supporting Information). On the other hand, in such colloidal domain, smaller charged particles reach the surface easier and faster than bigger particles. It is obvious then that the overall film thickness is not necessarily correlated with the ZnO particle size.

2.2. Fabrication of the Polymer BHJ Solar Cells

Thin-film BHJ solar cells with an inverted configuration of ITO/ZnO/PBDTTPD: $PC_{71}BM/MoO_3/Ag$ were fabricated with ZnO/PAA ETLs prepared by the LbL technique. Cells with optimized active layers of PBDTTPD:$PC_{71}BM$ in a blend ratio of 1:1.5 (wt/wt) were cast from chlorobenzene (CB) with 5% (v/v) of the processing additive 1-chloronaphthalene (CN).

Figure 3a shows the UV–vis absorption spectrum of the BHJ device. The spectrum shows the absorption peak of ZnO NPs at ≈365 nm while the whole absorption range up to 700 nm indicates the absorption of the polymer-fullerene active layer. The AFM height image (Figure 3b) shows the polymer BHJ after casting the active layer. As is apparent, the active layer filled the porous structure of the ZnO film. This resulted in a decrease in RMS roughness of the surface from 14.2 to 8.2 nm of the ZnO/PAA film before and after coating with the active layer, respectively. Although the pores are mostly filled with the active layer, the decrease in surface roughness is as not dramatic as in our previous work with PbS quantum dots (QDs) in which the surface roughness of a 61-nm thick ZnO layer decreased from 18.8 to 1.5 nm upon coating with PbS QDs.[36] This smaller decrease is likely due to the fact that the polymer chains are soft and will follow the surface architecture of the rough ZnO underneath.

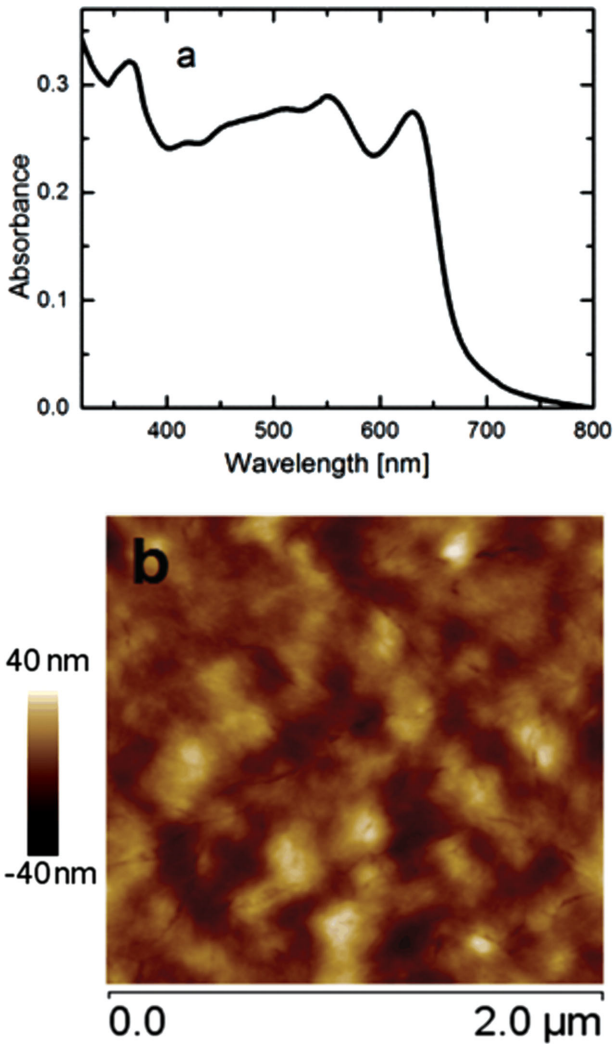

Figure 3. a) The UV–vis absorption spectrum of a polymer BHJ on top of a five-bilayer ZnO/PAA thin film. b) The corresponding AFM height image of the same device showing the active polymer layer covering the surface of the ZnO nanoparticles and filling the pores in between.

2.3. Solar Cell Performance

Figure 4a shows the efficiency of the as-prepared and annealed films as a function of the number of bilayers (n). The efficiency results show a strong dependence on the number of bilayers, until a plateau is reached at four bilayers. A further increase in the number of bilayers does not induce further efficiency improvements. Interestingly, as-prepared ETLs yield PCE values that are approximately a factor of 2 greater than those of thermally annealed films treated under atmospheric conditions. As shown in **Table 1**, as-prepared ETL solar cells achieved high PCEs of ≈5.6% (Max.: 6%) with four bilayers of ZnO/PAA deposited by LbL with a thickness of 25 nm. These devices combined a FF of 55% and comparably high J_{SC} of more than 12 mA cm^{-2}. Meanwhile, solar cell devices with thermally annealed ETLs at 60, 80, 100, 200, and 300 °C (in a nitrogen atmosphere inside a glovebox) with the same number of bilayers achieved lower V_{OC}, J_{SC}, and FF than those of the as-prepared ETLs. This result indicates that annealing is not required for ETLs prepared by LbL and that in this case annealing does not help to improve device efficiency.

Figure 4b shows the efficiencies of devices using as-prepared LbL and sputtered ETLs as a function of film thickness. Sputtered ETLs have a slightly higher efficiency than LbL films at lower thicknesses, whereas LbL ETLs yield higher efficiencies at higher thicknesses. **Table 2** summarizes the device results with ZnO-sputtered interlayers. In fact, the maximum performance achieved with an optimized sputtered thickness of 10 nm is PCE of ≈4.6% (Max.: 5.1%). This lower performance compared with the LbL deposition mainly comes from a lower FF, which could arise from the difference in the interfacial contact with the active layer, considering that the surface roughness of a sputtered ZnO film is about 2 nm. The current density–voltage (J–V) curves and the external quantum efficiency (EQE) spectra of optimized LbL and sputtered ETL-deposited devices are shown in Figure 4c,d, respectively. The EQE response is the highest in the range of 350–650 nm, consistent with the distinct onsets of absorption of the polymers, which are within 65%–70%; this observation is in agreement with the device J_{SC} values obtained (>12 mA cm^{-2}). Furthermore, the EQE integration of the best device using sputtered ZnO and solution-processed LBL ZnO/PAA have values of 12.0 vs 11.8 mA cm^{-2}, respectively, which are close to the average J_{SC} obtained on the J–V curve (11.9 ± 0.3 and 12.1 ± 0.4 mA cm^{-2}, respectively). The higher PCE of the solution-processed ZnO/PAA comes essentially from the higher fill factor with respect to the sputtered ZnO (54 ± 1 vs 46 ± 3) and the slightly higher V_{OC} (0.86 ± 0.1 vs 0.84 ± 0.1 V). This indicates that the estimated PCE of the devices are reliable. In Figure 4d, a small difference in the absorption feature between the ZnO/PAA ETLs prepared by the LbL technique and that prepared by the sputtering technique was observed in the UV region. We considered that the spectral mismatch is due to the absorption of different amounts of ZnO nanoparticles in the ZnO ETL prepared by the two techniques.[36]

Thermal annealing of ZnO ETL in air or in a glovebox resulted in lowering the solar cell efficiency as seen in Figure 4a. To understand the underlying reasons, we conducted X-ray photoelectron spectroscopy (XPS) and attenuated total reflection Fourier-transform infrared (ATR-FTIR) experiments on the ZnO/PAA thin films before and after annealing in air. As can be seen in Figure S3 (Supporting Information), no change in the bandgap of the ZnO NP is observed upon annealing. In addition, AFM height images do not exhibit a pronounced morphology or surface roughness change before and after annealing (see Figure S4, Supporting Information).

XPS C1s spectra (**Figure 5**a) show that the ZnO/PAA film has about 10% less overall carbon content after annealing. It should be noted that the degradation of PAA has been reported to start partially (≈7%) at 300 °C.[45] It is well known that steady-state infrared experiments can give insights into the local interactions between donor and acceptor moieties.[46] Figure 5b shows clearly that the carboxylate group is broadened (due to charge delocalization) and downshifted by about 11 cm^{-1} after annealing, providing a clear signature for the electrostatic binding of the free carboxylate to the surface of ZnO NPs. Here, we infer that before annealing, these free carboxylates with their negative charges drive the electrons to the ZnO

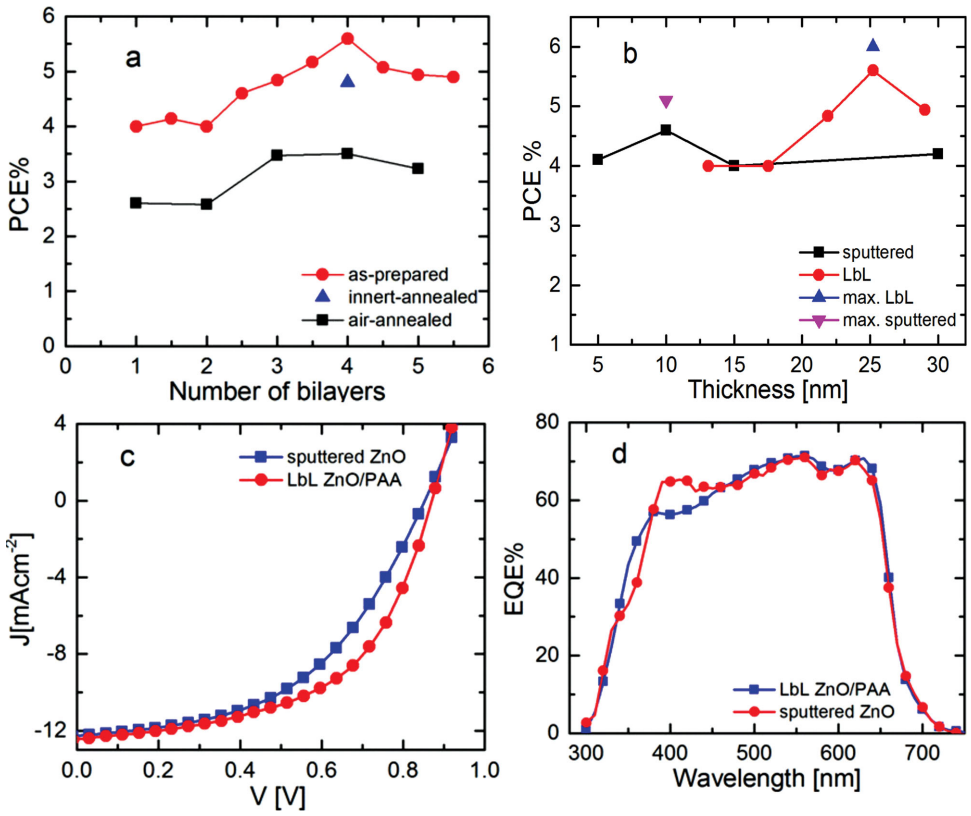

Figure 4. Inverted BHJ solar cells fabricated from the PBDTTPD derivatives, under AM1.5G illumination; cast from CB, with 5% (v/v) CN additive showing a) solar cell PCEs of the as-prepared and annealed ETLs as a function of the number of layers, b) PCE as a function of ETL thickness, c) characteristic *J–V* curves and d) external quantum efficiency (EQE) spectra of sputtered and LbL ZnO/PAA ETL-containing devices.

surface by means of repulsion forces. After annealing, conformational changes take place in the polyelectrolyte chain, and some of the free carboxylates bind electrostatically to the ZnO surface as indicated in the IR data, thus decreasing the effective repulsion force to drive the electrons to the surface of the ZnO layer. In addition, because of the binding mode and the conformational changes in the polyelectrolyte chain, it can be assumed that some of the active sites on the surface of the ZnO NP are no longer available as a pathway for the electrons to percolate. Electrostatic binding of free carboxylate together with the increased oxygen defects after annealing in air could contribute to the decreased device efficiency of the corresponding devices. It is worth pointing out that the device efficiency is also lower after annealing in a nitrogen environment compared to that of the as-prepared film, but higher than that of the air-annealed film, indicating that oxygen defects created after annealing in air can be considered as a major source of trap states, resulting in the low conversion efficiency after annealing.

Table 1. PV performance of the PBDTTPD in inverted BHJ devices with $PC_{71}BM$ and LbL ZnO/PAA ETL after light soaking.

Annealing	J_{SC} [mA cm^{-2}]	V_{OC} [V]	FF [%]	Avg. PCE [%]	Max PCE [%]
None	12.1 ± 0.4	0.86 ± 0.1	54 ± 1	5.6	6.0
60 °C/1 h	11.2 ± 0.3	0.83 ± 0.1	46 ± 3	4.3	4.7
80 °C/1 h	12.0 ± 0.2	0.74 ± 0.1	39 ± 3	3.4	3.6
100 °C/1 h	11.6 ± 0.3	0.64 ± 0.1	40 ± 4	3	3.4
200 °C/1 h	11.3 ± 0.5	0.77 ± 0.1	49 ± 4	4.3	4.7
300 °C/1 h	11.1 ± 0.4	0.81 ± 0.1	53 ± 3	4.8	5.3

3. Conclusion

In conclusion, we have shown that the layer-by-layer assembly of ZnO NPs and PAA under ambient conditions is a simple and effective approach to efficient inverted BHJ polymer solar cells. Following this approach, we demonstrated devices with ≈6.0% PCE, exceeding the PCE values of devices with ZnO interlayers deposited via conventional sputtering methods. Depositing ZnO interlayers by the LbL approach is advantageous over

Table 2. PV performance of the PBDTTPD in inverted BHJ devices with $PC_{71}BM$ and sputtered ZnO after light soaking.

ZnO sputtered thickness [nm]	J_{SC} [mA cm^{-2}]	V_{OC} [V]	FF [%]	Avg. PCE [%]	Max PCE [%]
5	11.9 ± 0.4	0.78 ± 0.1	44 ± 5	4.1	4.8
10	11.9 ± 0.3	0.84 ± 0.1	46 ± 3	4.6	5.1
15	11.7 ± 0.3	0.82 ± 0.1	42 ± 4	4.0	4.6
20	11.3 ± 0.5	0.82 ± 0.1	46 ± 4	4.2	4.9

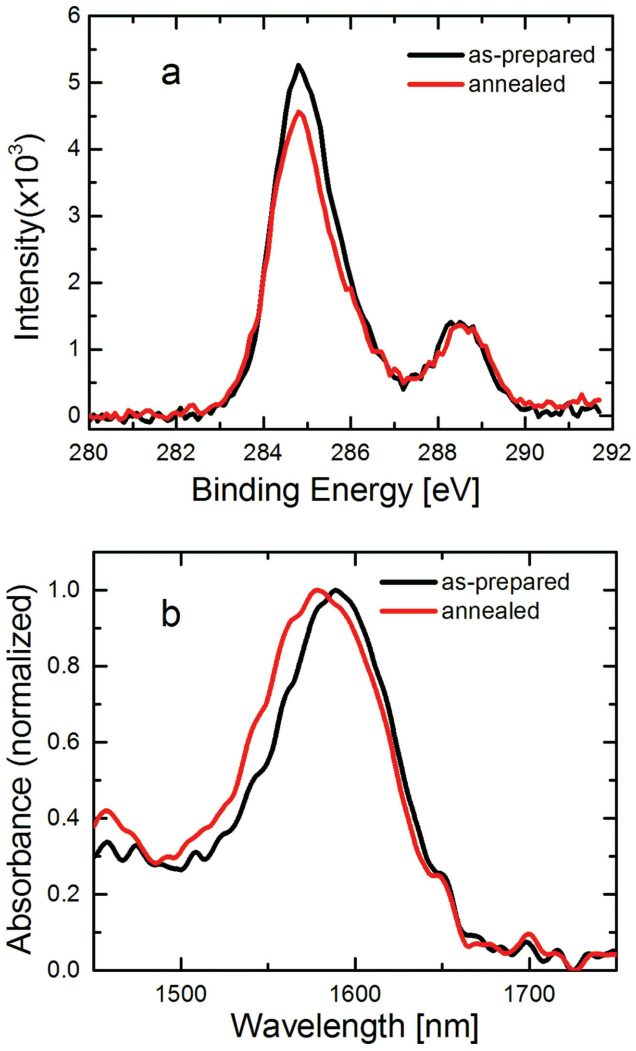

Figure 5. a) C1s XPS spectra of a four-bilayer ZnO/PAA as-prepared and annealed thin film at 300 °C in air for 1 h; b) ATR-FTIR spectra of the as-prepared and annealed ZnO/PAA films showing the band of the free carboxylate group.

other methods because it does not require any postprocessing thermal annealing step and, in turn, it is applicable to flexible devices. In addition, the use of aqueous solvents minimizes the environmental footprint of the deposition process. The LbL-deposited ZnO/PAA platform is expected to be applicable to any inverted polymer-fullerene BHJ device as well as to other solar-cell architectures.

4. Experimental Section

Preparation of ZnO ETL: The solar cells were prepared on glass substrates with tin-doped indium oxide (ITO, 15 Ω sq^{-1}) patterned on the surface. The substrates were first immersed in an ultrasonic bath of diluted Extran 300 for 15 min, then rinsed in flowing deionized water for 5 min before being sonicated for 15 min in 0.1 M NaOH solution and rinsed with ultrapure water. This was followed by sonication in successive baths of isopropanol and acetone for 15 min each. Finally, the substrates were dried with pressurized nitrogen. Next, 0.5 g L^{-1} solutions of polyallylamine hydrochloride (PAH) (15 000 g mol^{-1}) and polyacrylic acid (PAA) (15 000 g mol^{-1}, 35% as sodium salt in water) were prepared in ultrapure water with the addition of 0.1 M NaCl. The ZnO NP dispersion (stabilized by cationic surfactant 3-aminopropyl triethoxysilane, 50 wt% in water, size < 100 nm) was diluted at a concentration of 0.1 wt% in ultrapure water. All chemicals were purchased from Sigma-Aldrich. For the LbL coating, substrates were first immersed for 20 min in PAH solution in order to coat one PAH layer to facilitate adsorption of the negatively charged PAA. The LbL coating was followed by immersion of substrates for 10 min in PAA and ZnO dispersions and consequently with three rinsing steps in ultrapure water for 2 min each. Finally, the films were dried with nitrogen after completion of the immersion cycles.

Characterization: The size of ZnO NPs was determined from TEM imaging. Thicknesses and refractive indices of thin films were measured by a spectroscopic ellipsometer (M2000, J. A. Wollam Co. Inc.) at variable incidence angles of 55°–65° with increments of 5°. The thicknesses and refractive indices were calculated by fitting the data to a Cauchy model.[47] AFM images were recorded (Dimension Icon microscope, Veeco) in the tapping mode under ambient conditions. Additionally, the thicknesses of the thin films were measured by AFM step analysis. Absorption spectra were recorded by a Cary5000 spectrometer (Agilent Technologies). XPS studies were carried out in a Kratos Axis Ultra DLD spectrometer equipped with a monochromatic Al Kα X-ray source (1486.6 eV) operating at 150 W, a multichannel plate and delay line detector under a 1.0×10^{-9} Torr vacuum. Binding energies were referenced to the C1s binding energy of adventitious carbon contamination, which was taken to be 284.8 eV. ATR-FTIR spectra were recorded on an FTIR spectrometer (Thermo iS10), reflectance cell from (HARRICK VariGATR).

Device Fabrication: All active layer solutions were prepared in a glovebox using PBDTTPD and $PC_{71}BM$ purchased from SOLENNE. PBDTTPD and $PC_{71}BM$ were dissolved in chlorobenzene (containing 5% (v/v) of 1-chloronaphthalene (CN) additive) and the solutions were stirred overnight at 110 °C. Optimized devices were prepared using a PBDTTPD:$PC_{71}BM$ in a ratio of 1:1.5 (by weight), with a concentration of 20 mg mL^{-1}. The effects of various solvents, solution concentrations, additive concentrations, and blend ratios on device performance were examined. The active layers were spin-cast from the solutions at 90 °C at an optimized speed for 45 s, using a programmable spin coater from Specialty Coating Systems (Model G3P-8), resulting in a film thickness of 100–120 nm. The samples were then dried at room temperature for 1 h. Next, the samples were placed in a thermal evaporator to evaporate the 4 nm thick molybdenum oxide at 0.5 Å s^{-1} and the 80 nm thick silver electrodes at 3 Å s^{-1}, at a pressure less than 1×10^{-7} Torr. Following electrode deposition, the samples underwent *J–V* testing. *J–V* measurements of solar cells were performed in a glovebox with a Keithley 2400 source meter and an Oriel Sol3A Class AAA solar simulator calibrated to 1 sun, AM1.5 G, with a KG-5 silicon reference cell certified by Newport. The external quantum efficiency (EQE) measurements were performed at zero bias by illuminating the device with monochromatic light supplied from a Xenon arc lamp in combination with a dual-grating monochromator. The number of photons incident on the sample was calculated for each wavelength by using a silicon photodiode calibrated by NIST.

Supporting Information

Supporting Information is available from the Wiley Online Library or from the author.

Acknowledgements

M.E. and A.E.L. contributed equally to this work. The research reported here was supported by King Abdullah University of Science and Technology.

Received: August 4, 2014
Revised: November 27, 2014
Published online: February 4, 2015

[1] B. O'Regan, M. Grätzel, *Nature* **1991**, *353*, 737.
[2] K. Ramanathan, M. A. Contreras, C. L. Perkins, S. Asher, F. S. Hasoon, J. Keane, D. Young, M. Romero, W. Metzger, R. Noufi, J. S. Ward, A. Duda, *Prog. Photovoltaics: Res. Appl.* **2003**, *11*, 225.
[3] K. L. Chopra, P. D. Paulson, V. Dutta, *Prog. Photovoltaics: Res. Appl.* **2004**, *12*, 69.
[4] F. Fthenakis, J. E. Mason, K. Zweibel, *Energy Policy* **2009**, *37*, 387.
[5] I. Repins, M. A. Contreras, B. Egaas, C. DeHart, J. Scharf, C. L. Perkins, B. To, R. Noufi, *Prog. Photovoltaics: Res. Appl.* **2008**, *16*, 235.
[6] A. Hagfeldt, M. Grätzel, *Acc. Chem. Res.* **2000**, *33*, 269.
[7] A. Hagfeldt, G. Boschloo, L. Sun, L. Kloo, H. Pettersson, *Chem. Rev.* **2010**, *110*, 6595.
[8] F. Odobel, Y. Pellegrin, J. Warnan, *Energy Environ. Sci.* **2013**, *6*, 2041.
[9] H. Hoppe, N. S. Sariciftci, in *Photoresponsive Polymers II*, (Eds: S. R. Marder, K.-S. Lee), Springer, Berlin, Heidelberg **2008**, Vol. *214*, p 1.
[10] G. Li, R. Zhu, Y. Yang, *Nat. Photonics* **2012**, *6*, 153.
[11] A. Kongkanand, K. Tvrdy, K. Takechi, M. Kuno, P. V. Kamat, *J. Am. Chem. Soc.* **2007**, *130*, 4007.
[12] P. V. Kamat, *J. Phys. Chem. C* **2008**, *112*, 18737.
[13] A. O. El-Ballouli, E. Alarousu, M. Bernardi, S. M. Aly, A. P. Lagrow, O. M. Bakr, O. F. Mohammed, *J. Am. Chem. Soc.* **2014**, *136*, 6952.
[14] J. Bouclé, H. J. Snaith, N. C. Greenham, *J. Phys. Chem. C* **2010**, *114*, 3664.
[15] W. J. E. Beek, M. M. Wienk, R. A. J. Janssen, *Adv. Mater.* **2004**, *16*, 1009.
[16] J. A. Anta, E. Guillén, R. Tena-Zaera, *J. Phys. Chem. C* **2012**, *116*, 11413.
[17] G. Li, V. Shrotriya, J. Huang, Y. Yao, T. Moriarty, K. Emery, Y. Yang, *Nat. Mater.* **2005**, *4*, 864.
[18] J. Y. Kim, K. Lee, N. E. Coates, D. Moses, T.-Q. Nguyen, M. Dante, A. J. Heeger, *Science* **2007**, *317*, 222.
[19] Y. Liang, Z. Xu, J. Xia, S.-T. Tsai, Y. Wu, G. Li, C. Ray, L. Yu, *Adv. Mater.* **2010**, *22*, E135.
[20] J. You, L. Dou, K. Yoshimura, T. Kato, K. Ohya, T. Moriarty, K. Emery, C.-C. Chen, J. Gao, G. Li, Y. Yang, *Nat. Commun.* **2013**, *4*, 1446.
[21] W. U. Huynh, J. J. Dittmer, A. P. Alivisatos, *Science* **2002**, *295*, 2425.
[22] A. M. Peiro, P. Ravirajan, K. Govender, D. S. Boyle, P. O'Brien, D. D. C. Bradley, J. Nelson, J. R. Durrant, *J. Mater. Chem.* **2006**, *16*, 2088.
[23] M. M. Lee, J. Teuscher, T. Miyasaka, T. N. Murakami, H. J. Snaith, *Science* **2012**, *338*, 643.
[24] M. A. Loi, J. C. Hummelen, *Nat. Mater.* **2013**, *12*, 1087.
[25] S. Schumann, R. D. Campo, B. Illy, A. C. Cruickshank, M. A. McLachlan, M. P. Ryan, D. J. Riley, D. W. McComb, T. S. Jones, *J. Mater. Chem.* **2011**, *21*, 2381.
[26] Y. Sun, J. H. Seo, C. J. Takacs, J. Seifter, A. J. Heeger, *Adv. Mater.* **2011**, *23*, 1679.
[27] H.-Y. Park, D. Lim, K.-D. Kim, S.-Y. Jang, *J. Mater. Chem. A* **2013**, *1*, 6327.
[28] Y. Gao, I. Gereige, A. E. Labban, D. Cha, T. T. Isimjan, P. M. Beaujuge, *ACS Appl. Mater. Interfaces* **2014**, *6*, 2219.
[29] H. Cheun, C. Fuentes-Hernandez, Y. Zhou, W. J. Potscavage Jr., S.-J. Kim, J. Shim, A. Dindar, B. Kippelen, *J. Phys. Chem. C* **2010**, *114*, 20713.
[30] S. K. Hau, H.-L. Yip, N. S. Baek, J. Zou, K. O'Malley, A. K.-Y. Jen, *Appl. Phys. Lett.* **2008**, *92*, 253301.
[31] Y.-J. Kang, K. Lim, S. Jung, D.-G. Kim, J.-K. Kim, C.-S. Kim, S. H. Kim, J.-W. Kang, *Sol. Energy Mater. Sol. Cells* **2012**, *96*, 137.
[32] Z. Liang, Q. Zhang, O. Wiranwetchayan, J. Xi, Z. Yang, K. Park, C. Li, G. Cao, *Adv. Funct. Mater.* **2012**, *22*, 2194.
[33] D. C. Lim, W. H. Shim, K.-D. Kim, H. O. Seo, J.-H. Lim, Y. Jeong, Y. D. Kim, K. H. Lee, *Sol. Energy Mater. Sol. Cells* **2011**, *95*, 3036.
[34] L. K. Jagadamma, M. Abdelsamie, A. E. Labban, E. Aresu, G. O. N. Ndjawa, D. H. Anjum, D. Cha, P. M. Beaujuge, A. Amassian, *J. Mater. Chem. A* **2014**, *2*, 13321.
[35] D. Liu, T. L. Kelly, *Nat. Photonics* **2013**, *8*, 133.
[36] M. Eita, A. Usman, A. O. El-Ballouli, E. Alarousu, O. M. Bakr, O. F. Mohammed, *Small* **2014**, *11*, 112.
[37] C. Piliego, T. W. Holcombe, J. D. Douglas, C. H. Woo, P. M. Beaujuge, J. M. J. Fréchet, *J. Am. Chem. Soc.* **2010**, *132*, 7595.
[38] C. Cabanetos, A. E. Labban, J. A. Bartelt, J. D. Douglas, W. R. Mateker, J. M. J. Fréchet, M. D. McGehee, P. M. Beaujuge, *J. Am. Chem. Soc.* **2013**, *135*, 4656.
[39] J. A. Bartelt, J. D. Douglas, W. R. Mateker, A. E. Labban, C. J. Tassone, M. F. Toney, J. M. J. Fréchet, P. M. Beaujuge, M. D. McGehee, *Adv. Energy Mater.* **2014**, 4, 1301733.
[40] J. Warnan, C. Cabanetos, R. Bude, A. E. Labban, L. Li, P. M. Beaujuge, *Chem. Mater.* **2014**, *26*, 2829.
[41] J. Warnan, A. E. Labban, C. Cabanetos, E. T. Hoke, P. K. Shukla, C. Risko, J.-L. Brédas, M. D. McGehee, P. M. Beaujuge, *Chem. Mater.* **2014**, *26*, 2299.
[42] J. Warnan, C. Cabanetos, A. E. Labban, M. R. Hansen, C. Tassone, M. F. Toney, P. M. Beaujuge, *Adv. Mater.* **2014**, *26*, 4357.
[43] K. R. Graham, C. Cabanetos, J. P. Jahnke, M. N. Idso, A. E. Labban, G. O. N. Ndjawa, T. Heumueller, K. Vandewal, A. Salleo, B. F. Chmelka, A. Amassian, P. M. Beaujuge, M. D. McGehee, *J. Am. Chem. Soc.* **2014**, *136*, 9608.
[44] M. Eita, L. Wägberg, M. Muhammed, *J. Phys. Chem. C* **2012**, *116*, 4621.
[45] I. C. McNeill, S. M. T. Sadeghi, *Polym. Degrad. Stab.* **1990**, *29*, 233.
[46] M. J. Tan, S. Zhong, J. Li, Z. Chen, W. Chen, *ACS Appl. Mater. Interfaces* **2013**, *5*, 4696.
[47] H. G. Tompkins, E. A. Irene, *Handbook of Ellipsometry*, William Andrew Publishing, Norwich, NY **2005**.